IEEE Access
Multidisciplinary | Rapid Review | Open Access Journal

Received May 22, 2020, accepted June 3, 2020, date of publication June 8, 2020, date of current version June 24, 2020.

Digital Object Identifier 10.1109/ACCESS.2020.3000564

Simulation-Assisted Design of a Bidirectional Wireless Power Transfer With Circular Sandwich Coils for E-Bike Sharing System

CHIH-CHIA LIAO[1], (Graduate Student Member, IEEE), MING-SHI HUANG[1], (Member, IEEE), ZHENG-FENG LI[1], (Graduate Student Member, IEEE), FAA-JENG LIN[2], (Fellow, IEEE), AND WEI-TING WU[1]

[1]Department of Electrical Engineering, National Taipei University of Technology, Taipei 10608, Taiwan
[2]Department of Electrical Engineering, National Central University, Chungli 32001, Taiwan

Corresponding author: Ming-Shi Huang (mingshi.huang@gmail.com)

ABSTRACT A wireless power transfer (WPT) system with bidirectional power flow control for charging batteries and drawing electric power from batteries is presented in this paper for e-bike sharing applications. The proposed WPT consists of a bidirectional DC-DC converter and a sandwiched coil set, which includes primary winding with ferrite pad in charging stations and a movable secondary coil without ferrite pad, which is inserted into the primary coils to receive or transmit energy, on the e-bike. Hence, the proposed coil set could provide high coupling factor, better tolerance of misalignment, and a compact size that enables easy installation in the current mechanism of bike-sharing systems. The Maxwell 3D is adopted to design coil sets, which are based on the known resistance of Litz wire, and the effect of the ferrite pad and misalignment are analyzed to achieve good performance. To select a suitable converter, the characteristics of predesigned coils are simulated using Maxwell 3D, MATLAB and PSIM. Then, a full-bridge CLLC converter with the same resonant frequency for charging and discharging modes is chosen to provide minimal loss by using the synchronous rectifier on the 48-V side and voltage gain without the loading effect. Finally, a digital signal processor-based digitally controlled CLLC converter is constructed to verify the performance of the proposed WPT, which can provide 200 to 48 V/500 W charging and discharging functions with constant current/constant voltage modes and fast-response current control. In addition, the maximum efficiency is 96% at 52 V and 75% rated load in charging mode.

INDEX TERMS Wireless power transfer (WPT), bidirectional DC-DC converter, e-bike sharing applications, sandwich coil, Maxwell 3D, full-bridge CLLC converter.

I. INTRODUCTION

Because of traffic congestion and to reduce CO_2 emissions, pedal electric bicycles (Pedelecs) are increasingly becoming popular in Europe recently. Germany has 30 million commuters, and many of them travel less than 10 km to work [1]. Hence, pedelecs benefit commuters by being good for the environment, stress free, fast, and flexible in traffic jams, as well as by promoting commuters' health [2]. In 2018, the estimated sales volume of electric bikes (e-bikes) neared 2.6 million units [3]. Moreover, e-bikes consume the least amount of CO_2 per mile, from 2.6 to 5.0 g according to the energy source of charging stations, compared with 75 g for electric cars and 136 g for scooters [4]. Traditional bike-sharing systems are widely used for urban transport worldwide [4]–[7] and provide many advantages including decreased vehicle emissions and time saved from traffic congestion. More than 36,000 shared bikes and 840 stations [8] are in operation in the Taipei metropolitan area, and they are known as YouBikes, as displayed in Fig. 1(a). However, high temperatures in summer and traveling up hills may make users uncomfortable on pedal bikes powered manually.

E-bikes provide many advantages over conventional bikes because they move from battery power to assist human pedaling. Fig. 1(b) illustrates the Citi Bike in New York City, which provides pedal-assisted e-bikes with a speed up to 18 mph [9] and can effectively reduce commuting times and is friendly for elderly people [10]. To promote

The associate editor coordinating the review of this manuscript and approving it for publication was Narsa T. Reddy.

(a) (b)

FIGURE 1. Bike-sharing system: (a) YouBike in Taiwan [8]; (b) electric Citi Bike in New York City [9].

e-bikes for commuting and traveling in urban areas, the e-bike sharing system is proposed to overcome obstacles including high costs from e-bike purchases, maintenance, repairs, and charging e-bike batteries. However, charging the battery is a key problem of the e-bike sharing system. Therefore, inductive charging or wireless power transfer technologies were adopted [11], [12], which provide many advantages over conductive charging [12]–[14], some of which are as follows:

(i) Better safety while charging on rainy days and nights.

(ii) Better reliability and longer life cycle of the charging mechanism.

(iii) Addresses the tendency to forget to charge the battery after parking the e-bike.

The inductive charging system can be divided into loosely and tightly coupled structure according to the air gap between primary and secondary coils [13]. For electric vehicle (EV) applications, a loosely coupled structure may reduce the coupling factor and increase the effect of misalignment because of the larger air gap. Hence, many technologies improved the performance of loosely coupled inductive charging for EVs [15]–[18]. Moreover, heavy shielding materials are required because of large magnetic field leakage, which may also increase power loss and costs [19], [20]. Another type of inductive charging for EVs is a tightly coupled structure, which can improve system efficiency and reduce magnetic field leakage. General Motors proposed a tightly coupled inductive charger with an ultra-compact transformer for EVs, which can provide 120-kW charging power. The core was essentially an E–E, with a round center leg [21]. Researchers [22] proposed an EV charging system with a universal inductive interface. The design concept is based on a coaxial winding transformer and involves placing the core material of transformers outside vehicles. In [23], a new tightly coupled handheld resonant magnetic field (HH-RMF) charger operating at 20 kHz with a low electromagnetic field and high efficiency was proposed. An effective sandwich WPT presented in [24], which was used to recharge the battery of micro medical robots, provided 5 W for a cardiac pacemaker and exhibited 88% efficiency.

The application scenario of proposed bidirectional wireless charging system is presented in Fig. 2. The power grid provides the main power to DC-bus through an AC–DC converter. Since, the power management scenarios of e-bike sharing system are quite complex, this paper focuses on the design of bidirectional CLLC converter and sandwich coil design. Moreover, the proposed WPT involving the sandwich structure displayed in Fig. 3 provides the following benefits:

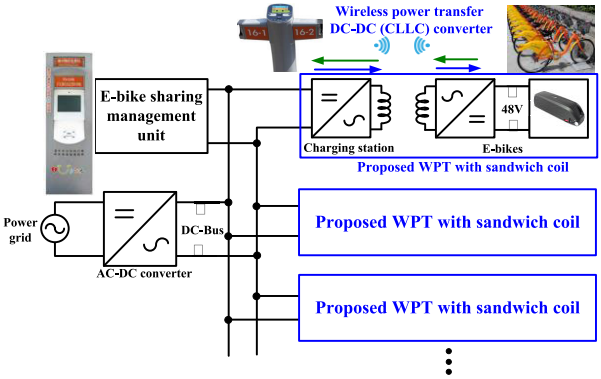

FIGURE 2. Application scenario of the proposed bidirectional WPT for e-bike sharing system.

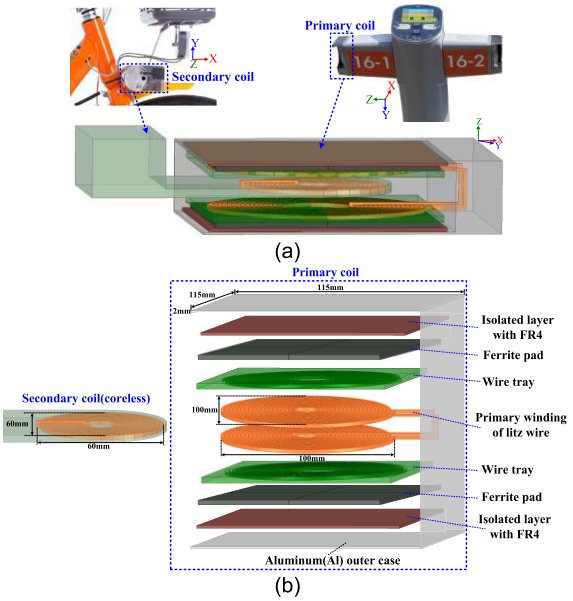

FIGURE 3. Proposed sandwich WPT in the e-bike sharing system: (a) installed position of primary and secondary coils; (b) exploded view.

(i) Compact size and coreless secondary coil to provide good reliability and light weight.

(ii) High coupling factor and better tolerance of misalignment between primary and secondary coils to enhance efficiency and keep the parameters variation small for good control.

(iii) Less flux leakage from the ferrite pad and aluminum case to reduce electromagnetic interference (EMI).

This paper derives the design procedure by using simulated software for self-inductance, coupling factor, misalignment effects, and voltage gain in advance for the converter design to reach needed functions with higher efficiency.

II. SYSTEM SPECIFICATIONS AND CONFIGURATION

The design baseline of WPT is used for the lock mechanism of the YouBike system [6] shown in Fig. 3(a). Primary and

TABLE 1. Specifications of the proposed WPT.

Parameter	Value
Rated power (W)	500
High side voltage(V)	200
Nominal battery voltage(V)	48
Battery operating voltage(V)	45-52
Maximum charging current(A)	10.5
Resonant frequency(kHz)	110
Air gap(mm)	5/5
Primary winding area(mm^2)	100 × 100
Secondary winding area(mm^2)	60 × 60
Aluminum outer case area(mm^2)	115 × 115

secondary coils are installed in the lock part of the parking post and bike, respectively. The lock mechanism area in the parking post is 115 mm × 115 mm. Fig. 3(b) presents the exploded view of primary and secondary coils. The primary coil is constructed from a gap between two coils, where both coils have an identical structure including a spiral winding of Litz wire, wire tray, ferrite pad, and FR4 insulation layer. The two windings are connected in series. Finally, the primary coil is placed inside an aluminum case fixed to the parking post. The secondary coil without ferrite cores consists of a spiral winding of Litz wire and a nonmetal outer case. The specifications of the proposed WPT system used to charge the 48-V Li-ion battery are listed in Table 1. The maximum charging and discharging current are set as 1 C-rated, and the air gap between primary and secondary winding on both side are 5 mm. To prolong the battery life cycle, the operation voltage of the battery is set from 45 V to 52 V [25].

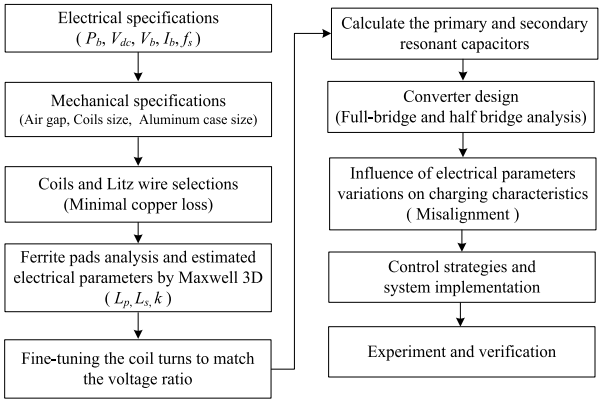

FIGURE 4. Proposed design process of the wireless charging system.

III. DESIGN OF THE PROPOSED WPT SYSTEM

Fig. 4 presents the design procedure of the proposed WPT system, which includes the primary/secondary coil set according to needed specifications and the converter for yielding the bidirectional power flow control. First, the turns of coils and the characteristics of the Litz wire are determined from the minimal copper losses of coils and power switches. Then, Maxwell 3D is adopted to design ferrite pads to yield suitable electrical parameters for the converter and analyze the magnetic shielding effect of the aluminum case. Finally, an active full-bridge circuit (FB–FB) is selected for the converter, and the effect of the electrical parameters variation on the charging voltage are discussed. Coupling factor k, primary self-inductance L_p, secondary self-inductance L_s, and the high-frequency AC resistance of coils that use Litz wires are the key parameters of WPT, which considerably affect system efficiency and the voltage operation range [13], [18], [26]–[28]. The main purpose of the proposed design rule is to optimize system efficiency by maximizing self-inductance and coupling factor under limitations from the voltage ratio, output-rated current, and the available area of coils and ferrite pads. To match the current mechanism and reduce the manufacturing cost, this paper uses circular spiral winding as primary and secondary coils, and the circular structure provides uniform flux distribution compared with the rectangular structure [29].

A. COILS AND LITZ WIRE SELECTIONS

To enhance efficiency, the coils of the proposed WPT comprise multiple strands Litz wire to reduce high-frequency AC resistance yielded by the skin effect. Hence, AC resistance is mainly determined by the total length of coil and the diameter of both strand and Litz wire. If the coupling factor and space limitation are the same, the larger diameter of Litz wire provides lower AC resistance. However, the available turns of coils are lower than that of Litz wire with a smaller diameter, which may reduce mutual inductance. Hence, the efficiency of coils with larger diameters of Litz wires is decreased due to increased magnetizing current. A study designing high quality factor coils to minimize copper loss with the same inductance by using Litz wire with a larger diameter was proposed in [30]. However, number of turns are reduced to decrease inductance under the limited coil area, which may have increased loss.

In this section, the selected procedure with Litz wires based on minimal copper loss is conducted to determine the diameter and match the area limitation. The Maxwell 3D and impedance analyzer are adopted to estimate inductances of Litz wire and coupling factor. Copper losses are calculated by (1), (2) with related current from simulated results of PSIM. Fig. 5 presents the equivalent circuits of the proposed WPT under charging and discharging modes, where a full-bridge CLLC converter is adopted.

The copper loss of the coils in charging mode (P_{ch_loss}) and discharging mode (P_{dis_loss}) can be derived as follows:

$$P_{ch\_loss}(3) = i_{rp}^2(\text{rms}) \times R_p + i_s^2(rms) \times R_s \quad (1)$$

$$P_{dis\_loss}(3) = i_{rs}^2(rms) \times R_s + i_p^2(rms) \times R_p \quad (2)$$

where

$i_{rp}(= i_{Lmp} + i_p)$: primary resonant current in charging mode.

$i_{rs}(= i_{Lms} + i_s)$: secondary resonant current in discharging mode.

R_p, R_s: primary and secondary winding resistance, respectively.

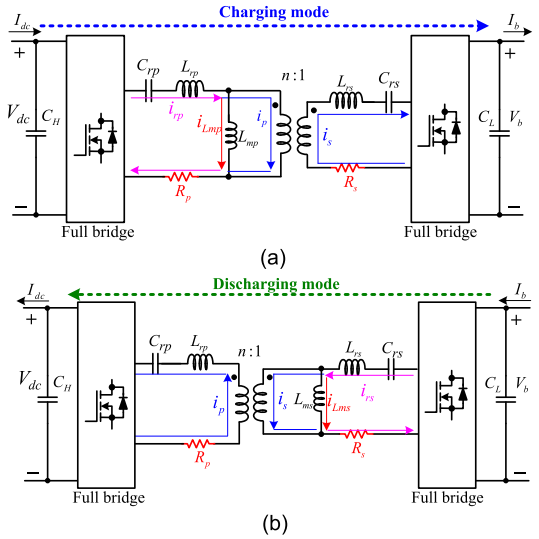

FIGURE 5. Equivalent circuits of the proposed WPT: (a) charging mode; (b) discharging mode.

i_{Lms}, i_{Lmp}: magnetizing current on primary and secondary side, respectively.

i_p, i_s: primary and secondary current, respectively.

Three diameters of Litz wires are compared under the following limitations and assumptions:

(i) The primary and secondary winding areas are near 100 mm × 100 mm and 60 mm × 60 mm, respectively, and simulated specifications depend on Table 1 with the maximum battery current of 10.5 A.

(ii) Maximum winding height is 3 mm; therefore, the maximum diameter of Litz wire is 3 mm.

(iii) The operating frequency of WPT is from 100 to 200 kHz, which leads the skin depth at 0.206 mm (at 100 kHz) and 0.146 mm (at 200 kHz), respectively. Hence, the wire gauge of Litz wire strands may have been larger than American wire gauge (AWG) 36 to reduce the skin effect. Litz wires contain AWG 44 (0.051 mm)/800 strands, AWG 38 (0.102 mm)/280 strands, and AWG 44 (0.051 mm)/1600 strands for comparison, respectively.

(iv) Because the simulated model of multi-strand Litz wires with different twisting methods are too complicated to yield accurate results by using Maxwell 3D [31], [32], the AC resistance of Litz wires are directly measured using the impedance analyzer WK6500B to determine the unit length resistance to calculate the resistance of the three Litz wires.

(v) The squared ferrite pads are added for simulation.

The simulated results of Litz wires with different diameters are shown in Table 2, and the following results could be determined:

(i) The Litz wire with AWG 44/800 strands provides the largest inductance to reduce the magnetizing current. Hence, the Litz wire with AWG 44/800 strands reaches small losses, including from the charging and discharging modes, and the smallest rated resonant current, which may have led to minimal loss and stress of power switches.

TABLE 2. Simulated results of Litz wires with different diameters for the proposed WPT (f_s = 110 kHz, V_{dc} = 200 V, V_b = 48V).

Litz wire specifications	2 mm AWG44/800 strands	2.2 mm AWG38/280 strands	3 mm AWG44/1600 strands
Primary coil			
Winding diameter	100 mm 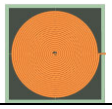	101 mm 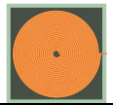	102 mm 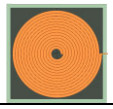
Turns	23	20.5	16
L_p (μH)	134.7	107	52.6
k	0.74	0.72	0.70
L_{mp} (μH)	99.7	77.0	36.8
i_{rp} (Arms)	4.1	4.7	8.3
Secondary coil			
Winding diameter	60 mm 	61 mm 	62 mm 
Turns	13N	11.5N	8.5N
L_s (μH)	6.75	5.22	2.79
L_{ms} (μH)	5.02	3.76	1.95
i_{rs} (Arms)	17.7	21.5	36.9
Measurement and calculation(at 110 kHz)			
R_p (mΩ)	112.8	86.9	41.9
R_s (mΩ)	20.7	18.7	7.4
P_{ch_loss} (W)	4.9	4.6	4.0
P_{dis_loss} (W)	7.4	9.3	10.4

(ii) The coupling factors of the three types of Litz wires are nearly the same because the coil areas of the three Litz wires are nearly the same, which is consistent with accepted theory [33].

Based on the aforementioned simulated and calculated results, the authors select the Litz wire with AWG 44/800 strands to design primary and secondary coils.

B. INFLUENCE OF FERRITE PAD AND PAD ALUMINUM (AL) CASE

To increase the coupling factor of the proposed WPT, ferrite pads are added on the case side of two primary coils. Area of ferrite pads may strongly influence the coupling factor and self-inductance. Hence, Maxwell 3D is used to analyze and estimate the optimal mechanical size of ferrite pads.

1) SELF INDUCTANCE AND COUPLING FACTOR WITH DIFFERENT AREA OF FERRITE PADS

Fig. 6 shows the simulated results of the self-inductance of primary and secondary coils versus different square ferrite widths W_{fe} with 2.5 mm thickness. The variation in the primary self-inductance is larger than that in the secondary self-inductance with an increasing width of the ferrite pad, as presented in Fig. 6(a). It is because the fixed air gap of the proposed sandwich structure makes the variation in secondary self-inductance remain small against an increasing ferrite width. The primary self-inductance can be derived as

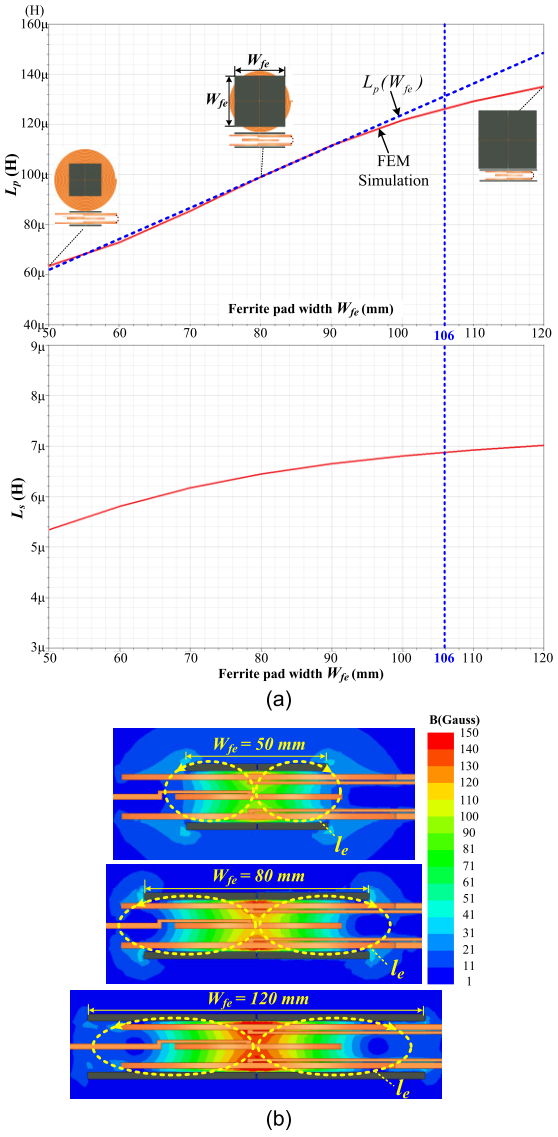

FIGURE 6. Simulated results of WPT characteristics versus ferrite pad width with 2.5 mm thickness: (a) self-inductance; (b) flux density distribution and flux path length l_e.

follows:

$$L_p = \frac{N^2}{\Re} = 0.5\mu N^2 \frac{W_{fe}^2}{l_e} \tag{3}$$

where $\Re$ is reluctance, μ is permeability, N and l_e are number of turns in primary winding and the length of the flux path, respectively.

A large width of ferrite pad may increase the length of flux path as presented in Fig. 6(b) because the magnetizing reluctance of ferrite is considerably smaller than that of air; hence, we could determine tendency $l_e \propto W_{fe}$. Then, the self-inductance of the primary coil could be derived as follows:

$$L_p(W_{fe}) \approx 0.5uN^2 k_1 W_{fe} \tag{4}$$

where $k_1 (= \frac{W_{fe}}{l_e})$ is near constant.

The changing slope of the coupling factor presented in Fig. 7 is slowing down when the ferrite pad width is larger

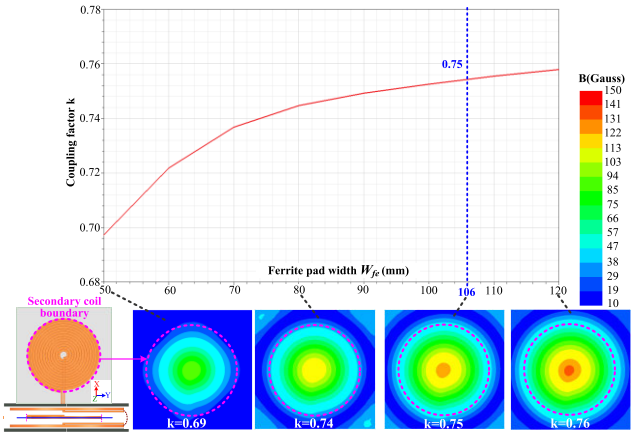

FIGURE 7. Simulated results of the coupling factor versus ferrite pad width with 2.5 mm thickness and flux density on the secondary coil.

than 80 mm. Moreover, the maximum flux density in center of secondary coil is less than 150 gauss because of the large air gap of WPT. This paper selects an 106-mm-wide ferrite pad near the boundary of case, which are assembled by eight 53 mm × 53 mm square ferrite pieces with MP2106 material [34] and 2.5 mm thickness to reduce costs, to provide 126 μH and 6.88 μH self-inductance for primary and secondary coils, respectively. The coupling factor between primary and secondary coils is 0.75.

2) SELF INDUCTANCE AND COUPLING FACTOR WITH DIFFERENT THICKNESS OF FERRITE PADS

The effect of ferrite pad thickness on coupling factor and self-inductance of the proposed coils are illustrated in Fig. 8. Wherein the maximum variation in self-inductance and coupling factor are less than 1.5% when the ferrite pad thickness is larger than 2 mm. Moreover, since only 1.1 mm and 2.5 mm thickness are available. The 2.5 mm thickness ferrite pad is selected, which has similar price as 1.1 mm thickness and can provide highly mechanical strength [34].

3) EFFECTS OF ALUMINUM (AL) CASE

Because of the eddy current effect on the aluminum case, the coupling factor and self-inductance slightly decrease, and simulated results are illustrated in Fig. 9 and Table 3. The effect of the Al case becomes minimized by increasing the width of the ferrite pad. Hence, the maximum variation of electrical parameters are less than 7% under the 106-mm-wide ferrite pad, and the required operating frequency could be achieved within the derived range of misalignment. By contrast, the fringing effect of the flux density presented in Fig. 10 is suppressed by the Al case, which may have led to decreased EMI.

C. FINE TUNING OF VOLTAGE RATIO

The design value of the voltage ratio between primary and secondary coils is 4.17, which is 200 V over 48 V. However, the voltage ratio is 4.47 from Maxwell 3D according to Table 2. To meet the voltage ratio, we could only reduce

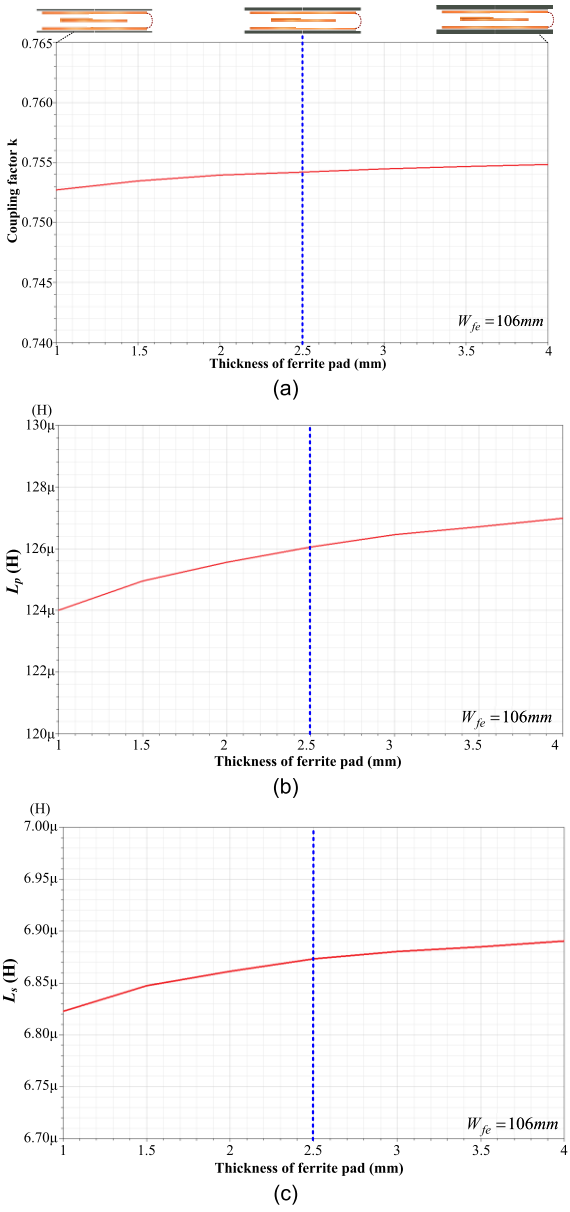

FIGURE 8. Simulated results of WPT characteristics versus thickness of ferrite pad with 106 mm width: (a) coupling factor; (a) self-inductance of primary coil; (b) self-inductance of secondary coil.

TABLE 3. Effect of Al case on WPT with a 106-mm-wide ferrite pad.

Conditions	Without Al case	With Al case
k	0.754	0.75
L_p (μH)	126	118
L_s (μH)	6.88	6.75
Voltage ratio	4.27	4.18
L_{rp} (μH)	31.2	29.5
C_{rp} (nF)	71	
f_{rp} (kHz)	107	110

primary winding turns instead of increasing turns of secondary winding due to limitations on the secondary area and

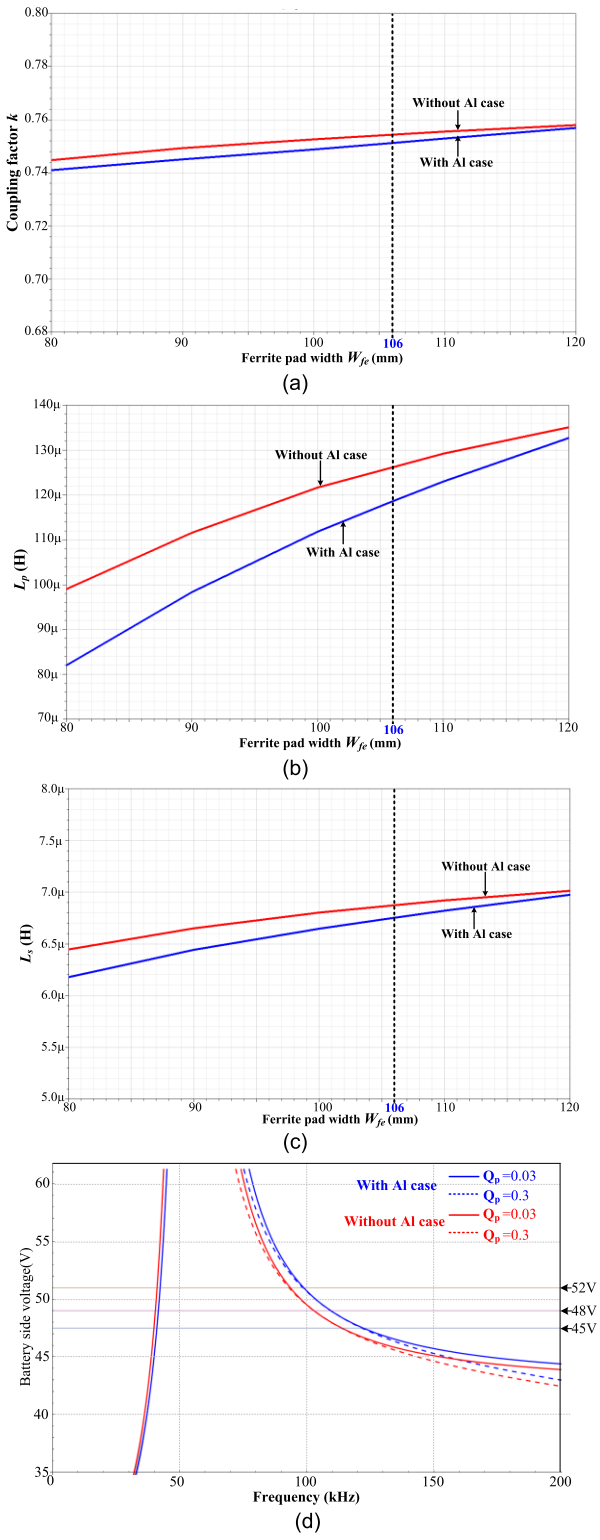

FIGURE 9. Simulated results of the Al case on the proposed WPT: (a) coupling factor: (b) self-inductance of primary coil; (c) self-inductance of secondary coil; (d) voltage gain with the 106-mm-wide ferrite pad.

height. Hence, fine-tuning the number of turns in primary winding is needed. Two approaches can achieve the desired voltage ratio by reducing turns: from the center and from the outer spiral winding. Fig. 11 reveals the simulated results and

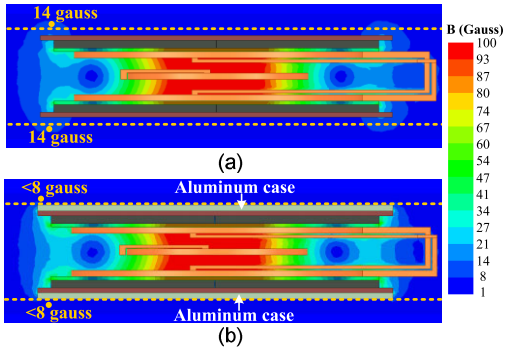

FIGURE 10. Fringing effect of flux density with and without Al case: (a) without Al case; (b) with Al case.

the winding area of these approaches to be nearly the same. Moreover, the center reduction approach may reduce the coupling factor more than the other approach. The coupling factor of the center reduction approach is decreased from 0.75 to 0.72 compared with outer reduction approach at the ferrite pad width of 106 mm. Then, this paper adopts the outer reduction approach to reach the desired voltage ratio with a 98 mm diameter of primary winding.

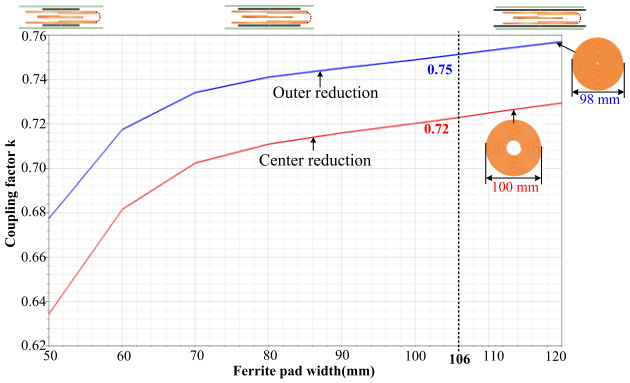

FIGURE 11. Simulated results of the coupling factor with the desired voltage ratio (= 4.17) from the two tuning approaches of primary winding.

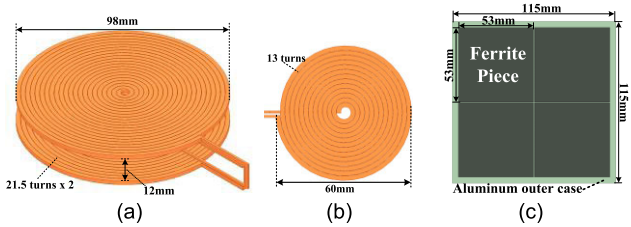

FIGURE 12. Mechanical structure and size of the proposed WPT: (a) primary winding; (b) secondary winding; (c) ferrite pad and aluminum case.

The mechanical structure and size of the proposed WPT are shown in Fig. 12. The parameters are presented in Table 3, and key points are summarized as listed:

(i) The 2-mm-diameter Litz wire with AWG 44/800 strands is employed to make primary and secondary windings with 21.5 turns/98 mm diameter and 13 turns/60 mm diameter, respectively, to achieve minimal losses. Moreover, the number of turns of primary winding are fine-tuned through the outer-reduction approach to reach the desired voltage ratio.

(ii) The ferrite pads of primary winding are constructed using eight square ferrite pieces with 53 mm width and 2.5 mm thickness to yield the maximum coupling factor under the predetermined diameter of windings.

D. FLUX DENSITY DISTRIBUTION OF FERRITE PADS

The flux saturation of ferrite materials may have induced parameters variation and increased loss. Because of a larger air gap with coreless secondary coil of the proposed sandwich structure, the flux density distribution on ferrite pads, as shown in Fig. 13. The maximum flux density on the ferrite pad is less than 440 gauss under the rated magnetizing current (peak value = 5 A), which is smaller than the saturation flux density of ferrite materials. Hence, the design does not need to consider the saturation effect, and the core loss may have been smaller than copper loss.

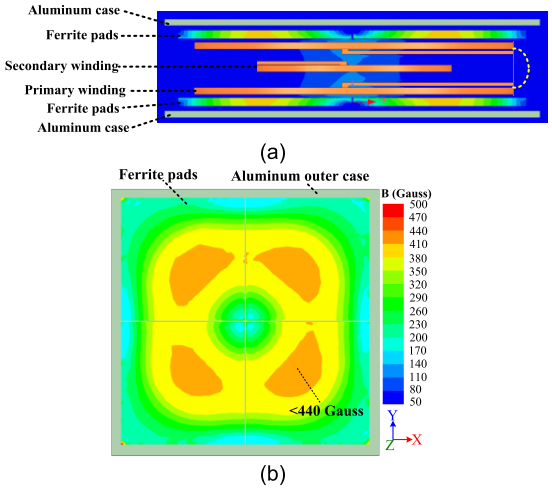

FIGURE 13. Flux density distribution of the proposed sandwich coil at rated magnetizing current: (a) between primary and secondary coils; (b) on surface of ferrite pads.

E. CONVERTER TOPOLOGY SELECTION

There are two simple and commonly used topologies of CLLC converter for isolated and bidirectional power flow applications [35], [36]. The equivalent circuit of the two topologies can be transferred to T-model in charging and discharging modes illustrated in Fig. 14 [37].

The DC voltage gain equations of CLLC converters in the charging mode ($|G_{\text{v.charge}}(f)|$) and discharging mode ($|G_{v.\text{discharge}}(f)|$) can be derived as in [35], [37] and rearranged:

$$\left|G_{\text{v.charge}}(f)\right| \left|\frac{v_{cd}}{v_{ab}}\right| = \frac{1}{n\sqrt{((1-\frac{1-k}{(\frac{f}{f_{rp}})^2})\frac{1}{k})^2+[Q_p(\frac{f}{f_{rp}})\frac{1}{\sqrt{1-k}}(\frac{1}{k}(1-\frac{1-k}{(\frac{f}{f_{rp}})^2}-k)]^2}} \tag{5}$$

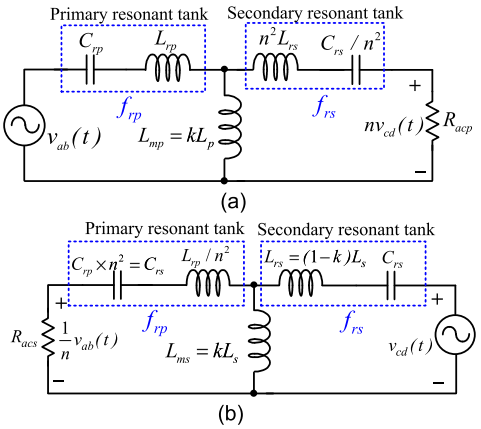

FIGURE 14. Equivalent model of the fundamental harmonics method: (a) charging mode (primary side); (b) discharging mode (secondary side).

$$\left|G_{v.\text{discharge}}(f)\right|\left|\frac{v_{ab}}{v_{cd}}\right| = \frac{n}{\sqrt{((1-\frac{1-k}{(\frac{f}{f_{rs}})^2})\frac{1}{k})^2+[Q_s(\frac{f}{f_{rs}})\frac{1}{\sqrt{1-k}}(\frac{1}{k}(1-\frac{1-k}{(\frac{f}{f_{rs}})^2}-k)]^2}} \tag{6}$$

where

v_{ab}, v_{cd}: primary and secondary ac voltage of the equivalent circuits, respectively.

$L_p = n^2 L_s$: self-inductance.

$L_{rp} = (1-k)L_p, L_{rs} = (1-k)L_s$: primary and secondary resonant inductance, respectively.

$C_{rp}(= \frac{C_{rs}}{n^2})$, C_{rs}: primary and secondary resonant capacitors, respectively.

$f_{rp}(= \frac{1}{2\pi\times\sqrt{(1-k)L_pC_{rp}}})$, $f_{rs}(= \frac{1}{2\pi\times\sqrt{(1-k)L_sC_{rs}}})$: Gprimary and secondary resonant frequency, respectively. $f_{rp} = f_{rs}$ in this design.

$n = \sqrt{\frac{L_p}{L_s}}$: Gvoltage ratio.

$R_{acp}(= \frac{8n^2}{\pi^2}\frac{V_b}{I_b})$, $R_{acs}(= \frac{8}{n^2\pi^2}\frac{V_{dc}}{I_{dc}})$: Gequivalent resistance of charging and discharging modes, respectively.

$Q_p(= \frac{1}{R_{acp}}\sqrt{\frac{L_{rp}}{C_{rp}}})$, $Q_s(= \frac{1}{R_{acs}}\sqrt{\frac{L_{rs}}{C_{rs}}})$: Gquality factor of charging and discharging modes, respectively.

$k = \frac{L_{mp}}{L_p} = \frac{L_{ms}}{L_s}$: Gcoupling factor.

If the converter is ideal, we can derive the following:

$$Q_p = Q_s \tag{7}$$

$$\left|G_{\text{v.discharge}}(f)\right| = n^2\left|G_{\text{v.charge}}(f)\right| \tag{8}$$

Hence, the proposed WPT will provide the same characteristic of voltage gain in charging and discharging mode according to (10) to simply the controller design. It means that one can design the controller in charging mode to use that in discharging mode.

A comparison of the characteristics of converter topologies with the same parameters in sandwich coils and the aluminum case are shown in Table 4, and simulated conditions depend on having a DC-bus voltage of 200 V, a battery voltage of 48 V, battery current of 10.5 A for charging and discharging modes, and switching frequency of 110 kHz. The parameters of primary and secondary coils are extracted using the Maxwell 3D, and the on-state resistance of high-voltage side and low-voltage side MOSFET are $R_{dson.H}$ and $R_{dson.L}$, respectively.

From comparison results listed in Table 4, we can summarize the following:

(i) The efficiency of HB–HB structure is lower at rated load condition because the resonant current is larger than that in the FB–FB structure in both charging and discharging modes.

(ii) The quality factor of HB–HB structure is higher compared with FB-FB because of the higher equivalent AC resistance [35], which resulted in a large slope change of the voltage gain curve at the heavy load, as displayed in Fig. 15.

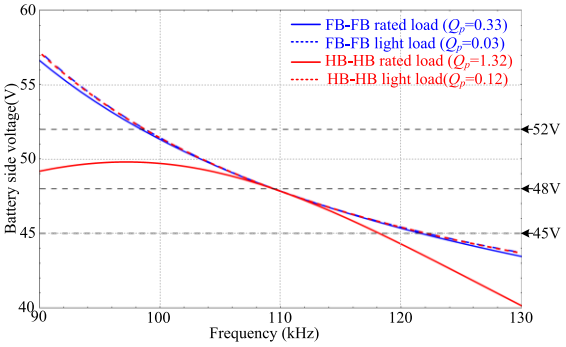

FIGURE 15. Voltage gain curve of FB-FB and HB-HB structure.

(iii) The HB-HB structure uses only four MOSFETs; however, the current rating is two times larger than that of the FB-FB structure, which increases current stress on MOSFETs and resonant capacitors.

(iv) Total conduction loss of the m pieces MOSFET on high voltage side and low voltage side are calculated as follow:

$$P_{loss,MOSFET} = \text{m} \times i^2_{MOSFET}(\text{rms})R_{dson} \tag{9}$$

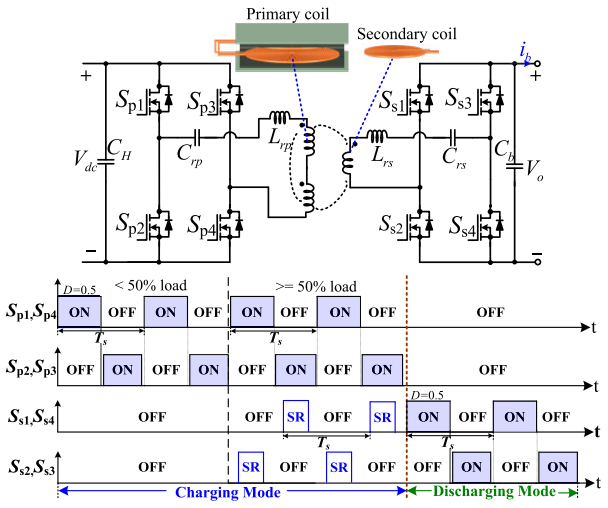

FIGURE 16. Full-bridge circuit (FB-FB) and switching control signals of the proposed WPT.

TABLE 4. Bidirectional CLLC topology comparison [35], [36].

Topology	FB-FB	HB-HB
Voltage ratio of coils (n : 1)	4.17:1	4.17:1
R_p (mΩ)	112.8	
R_s (mΩ)	20.7	20.7
Charging Mode		
i_{rp} (Arms)	4.28	5.81
i_s (Arms)	11.7	23.3
P_{ch_loss} (W)	4.9	15.0
High voltage side MOSFET loss(W)	$37R_{dson.H}$	$34R_{dson.H}$
Low voltage side MOSFET loss(W)	$274R_{dson.L}$	$543R_{dson.L}$
Discharging Mode		
i_{rs} (Arms)	18.0	24.4
i_p (Arms)	2.8	5.6
P_{dis_loss} (W)	7.6	15.9
High voltage side MOSFET loss(W)	$16R_{dson.H}$	$31R_{dson.H}$
Low voltage side MOSFET loss(W)	$648R_{dson.L}$	$595R_{dson.L}$

Depending on this analysis and the proposed charging specifications, this paper selects the FB–FB structure to achieve higher efficiency, and the switching control signals are illustrated in Fig. 16. The frequency control is adopted for S_{p1}-S_{p4} in charging mode and S_{s1}-S_{s4} in discharging mode. The synchronous rectifier (SR) control are only implemented for S_{s1}-S_{s4} under heavy load conditions in charging mode since the high voltage side current is smaller in discharging mode. Wherein, the primary and secondary resonant capacitors (C_{rp}, C_{rs}) are set as 71 nF and 1.234 μF respectively to reach the same resonant frequency (= 110 kHz).

F. EFFECTS OF MISALIGNMENT BETWEEN PRIMARY AND SECONDARY COILS

Misalignment is an inherent problem for WPT in vehicle applications and may cause variations in self-inductance and the coupling factor to change the voltage gain near the operating frequency. Hence, improving misalignment tolerance by using a magnetic and/or controller design is a key design problem of WPT. The maximum misalignment distance for this analysis are ±10 mm and ±2 mm for the *X*/*Y* and *Z*-axis, respectively. All the simulated results of misalignment are determined using Maxwell 3D.

The effect of misalignment, including the *X*-, *Y*-, and *Z*-axis, on self-inductance and the coupling factor are displayed in Fig. 17. Simulated results are briefly described as follows:

(i) The coupling factor and self-inductance of primary coil remain at the same value under *Z*-axis misalignment because the position of the coreless secondary coil does not affect primary winding, which are shown in Fig 17(a) and Fig 17(b), respectively.

(ii) Because of the spiral-type coil, the effect of *X*-axis and *Y*-axis misalignment on self-inductance and the coupling factor are the same. In this case, the coupling factor decreases from 0.75 to 0.69 when misalignment is from 0 to ± 10 mm.

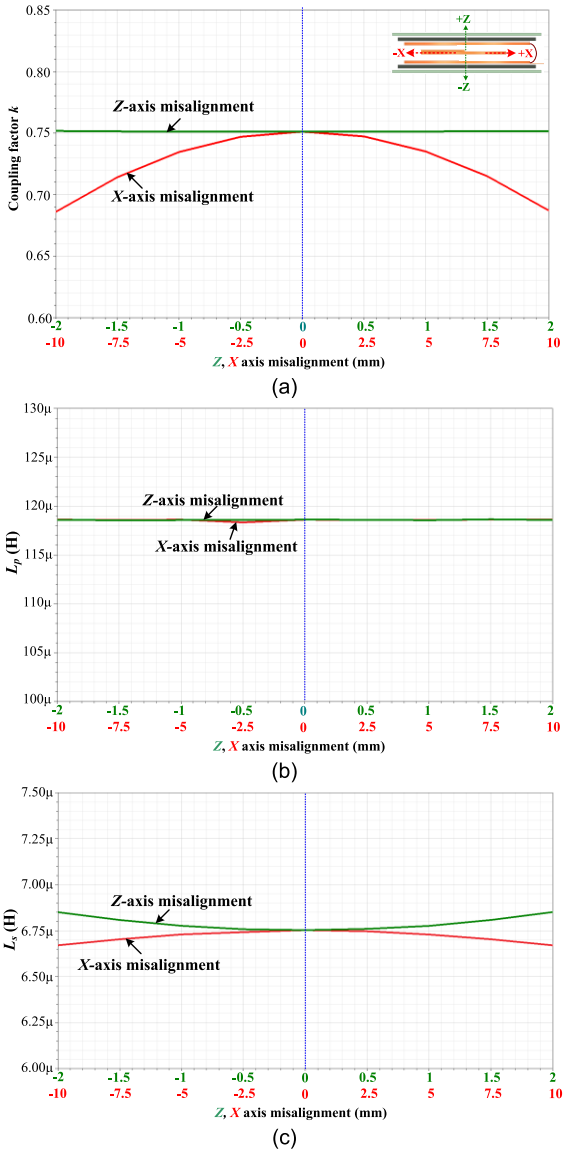

FIGURE 17. The influence of *Z*-axis and *XY*-axes misalignment on: (a) coupling factor; (b) primary self-inductance; (c) secondary self-inductance.

(iii) The maximum variation in self-inductance is less than 1% of the full alignment.

Because of the same resonant frequency both sides and the operating frequency being close to the resonant frequency, the voltage gain is near independent with loaded conditions. Moreover, the required charging voltage from 45 V to 52 V under worst-case misalignment, as illustrated in Fig. 18, could be reached by adjusting the operating frequency from 123 kHz to 90 kHz, respectively, at the rated load.

G. CONTROL METHODOLOGY

The function block diagram of the proposed WPT control scheme is illustrated in Fig. 19. The mode selection switch, SW, is adopted to let the battery be operated in charging or discharging mode. The control methodology is briefly described as follows:

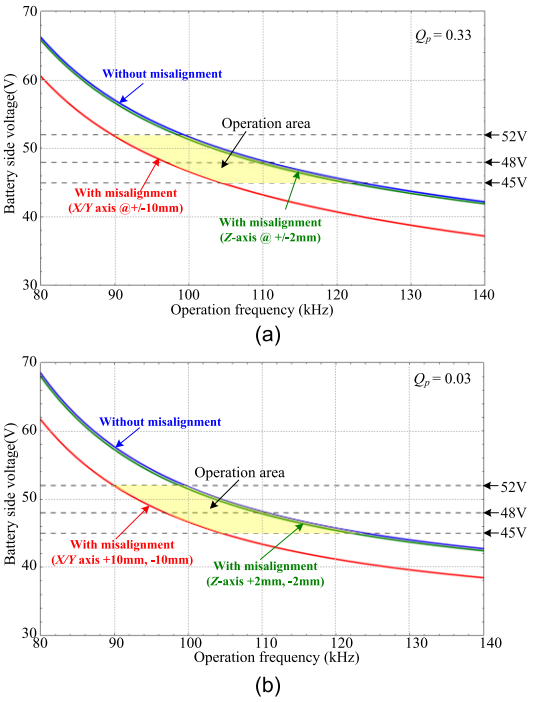

FIGURE 18. Simulated charging voltage under the worst-case of misalignment: (a) rated load; (b) 10% rated load.

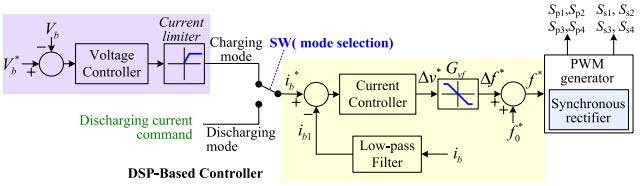

FIGURE 19. Control function block of the proposed WPT.

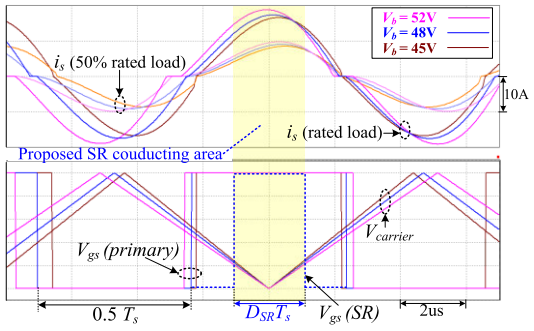

FIGURE 20. Simulated results of secondary current i_s and proposed SR with different operation voltage and loaded conditions.

1) CHARGING MODE

The controller, which connects a voltage controller with a current limiter to a current controller, provides constant voltage (CV) and constant current (CC) modes for charging the battery. The CC command is set by the current limited value. The SR control are implemented to reduce conduction loss with fixed duty cycle D_{SR} for secondary MOSFEFs without phase shift under different battery voltage and loaded conditions, which are based on simulated results of PSIM shown in Fig. 20 to simplify the complex phase shift control [38]. Wherein, D_{SR} is set as 0.28 to reduce 65% conduction loss at rated load and provides better reliability under load variation.

2) DISCHARGING MODE

Because the DC-bus voltage is controlled and kept a constant value by the AC-DC converter shown in the Fig. 2, the current controller is used to provide the needed discharging current.

3) CURRENT CONTROLLER

The operating frequency command f^* is generated as:

$$f^* = f_0^* + \Delta f^* \tag{10}$$

where f_0^* is the resonant frequency for both charging and discharging modes. The $\Delta f^*(= G_{vf} \times \Delta v^*)$ is yielded by voltage gain G_{vf} in Fig. 15 with limiter at resonant frequency.

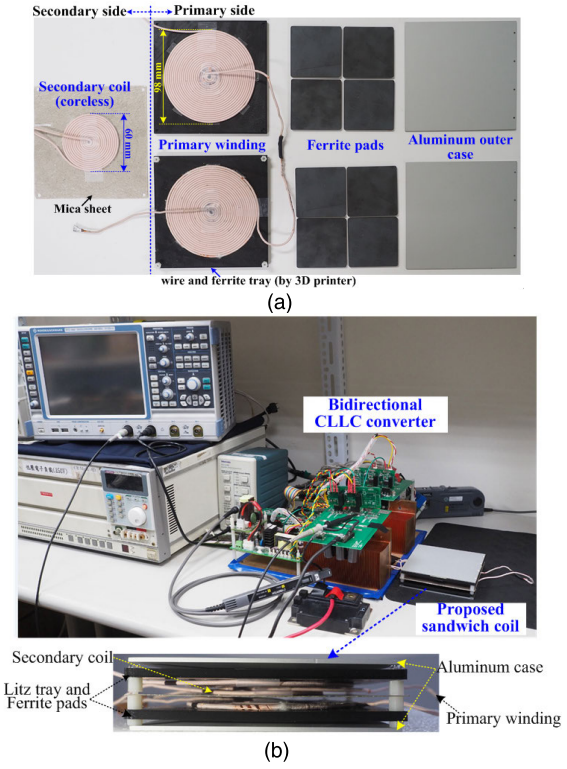

FIGURE 21. Experimental setup of the proposed WPT: (a) sandwich coils; (b) test setup.

IV. EXPERIMENTAL RESULTS

The experimental setup, specifications, and key parameters for implementing the proposed WPT are indicated in Fig. 21, Table 5, respectively. The efficiency of WPT under different loaded conditions are measured using Keysight PA2201. To obtain a highly accurate measurement of inductance and the coupling factor, the impedance analyzer WK 6500B is adopted.

TABLE 5. Key parameters of the implemented WPT.

Coil parameters	Primary side	Secondary side
Wire specifications	AWG44/800 strands Litz wire (2 mm)	
Turns	22+22	13.5
Self-inductance	116μH	7μH
AC resistance at 110k Hz	280mΩ	32mΩ
Coupling factor	0.76	
Resonant capacitors	71nF	1.234μF
MOSFET	R6046FNZ (600V/64mΩ)	IRF150P221 (150V/3.6mΩ)

TABLE 6. Simulated(Sim.) and experimental(Exp.) results of sandwich coils (AWG44/800 Strands of Litz Wire).

WPT Coils	k		L_p(μH)		L_s(μH)	
	Sim.	Exp.	Sim.	Exp.	Sim..	Exp.
Without Al case	0.75	0.76	126	124	6.88	7.30
Error	1.4%		1.6%		6.8%	
With Al case	0.75	0.76	118	116	6.75	7.01
Error	1.4%		1.7%		3.6%	

TABLE 7. Simulation(Sim.) and experimental(Exp.) results of coils under misalignment.

WPT Coils		k		L_p(μH)		L_s(μH)	
		Sim.	Exp.	Sim.	Exp.	Sim.	Exp.
Without misalignment		0.75	0.76	118.3	116.0	6.75	7.01
Z-axis	±1mm	0.75	0.76	118.3	115.8	6.78	6.95
	±2mm	0.75	0.76	118.3	115.7	6.85	6.92
X-axis	±5m	0.73	0.75	118.6	116.3	6.72	6.97
	±10mm	0.69	0.71	118.6	116.5	6.67	6.95
Error		< 2.9%		< 2.6%		< 4.2%	

A. CHARACTERISTICS OF WPT

1) WINDINGS PARAMETERS

Table 6 presents the simulated and experimental results of proposed sandwich coils, and the maximum error between simulated and experimental results is 3.6% with the Al case.

2) MISALIGNMENT OF Z AND X OR Y DIRECTION

The movable secondary coil is placed on the mica sheet with different positions of the X-axis, and the Z-axis misalignment is controlled by stacking layers of mica sheet with 1 mm thickness. Table 7 indicates that

(i) The misalignment in the Z-axis is nearly no influence on the electrical parameters of proposed coils.

(ii) Although the experimental coupling factor is reduced to 0.71 in the X-axis, which is 93.4% of the coupling factor without misalignment, the influence may have been mitigated by the closed loop controller.

(iii) The experimental results are close to simulated results with Maxwell 3D.

3) VOLTAGE GAIN

Fig. 22 shows the experimental and simulated results of the battery-side voltage under different loaded conditions.

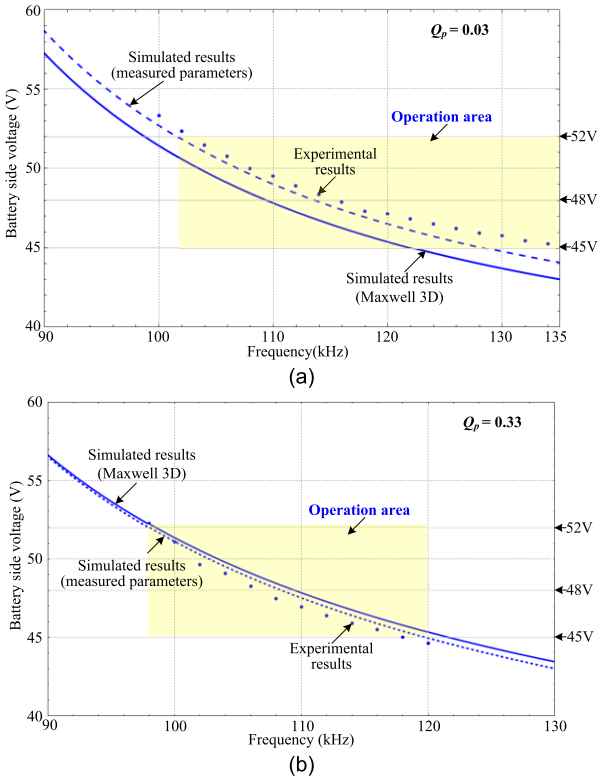

FIGURE 22. Experimental and simulated results of the battery-side voltage in charging mode (V_{dc} = 200 V): (a) light load (Q = 0.03); (b) rated load (Q = 0.33).

Simulated results are calculated using (7) with electrical parameters yielded and measured using Maxwell 3D and the impedance analyzer, respectively. Results indicate:

(i) Simulated results with measured electrical parameters close to experimental results.

(ii) Because of the higher resonant current harmonics in the light load, the maximum error between the simulated (parameters by Maxwell 3D) and experimental results is near 6%. By contrast, the maximum error in the heavy load is less than 3%.

Hence, electrical parameters simulated by Maxwell 3D could be used to simulate the output voltage and match well with experimental results before implementation to reduce the cost and time of trial and error.

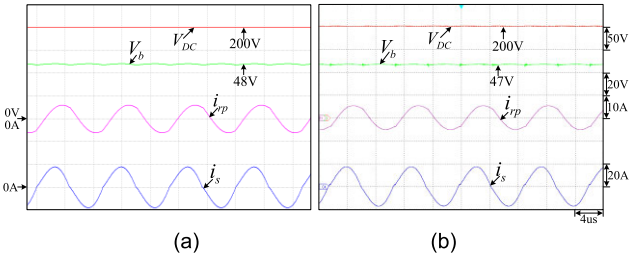

FIGURE 23. Experimental and simulated results at resonant frequency (V_{dc} = 200 V, R_L = 4.57 Ω): (a) PSIM simulation (f_{rp} = 110 kHz); (b) experiment (f_{rp} = 112 kHz).

4) RESONANT FREQUENCY

The resonant frequency is measured and presented in Fig. 23(a). The resonant frequency of experiment approaches 112 kHz with a minimal distortion of primary resonant currents i_{rp} and secondary transfer current i_s [39]. The measured results match the simulated results, as shown in Fig. 23(b), which are yielded by PSIM with measured electric parameters and the designed resonant frequency of 110 kHz. The experiment indicates that the simulated results of PSIM are considerably close to measurement results.

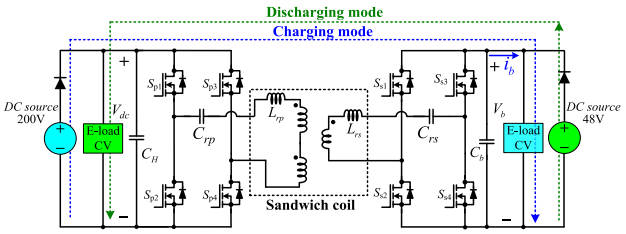

FIGURE 24. Test setup for the proposed WPT.

B. CONTROL PERFORMANCE

To measure the control performance of the proposed WPT, the test setup is presented in Fig. 24. Electronic loads under the CV mode, which is parallel and connected a DC power supply with a diode to block the reversed current, are added on both sides of the converter to simulate the DC-bus and battery.

1) ZERO VOLTAGE SWITCHING (ZVS) AND ZERO CURRENT SWITCHING (ZCS)

The measured results of ZVS on the high-voltage-side MOSFET and ZCS on the low-voltage-side MOSFET are shown in Figs. 25 and 26, respectively, which may have led to higher efficiency for the proposed WPT.

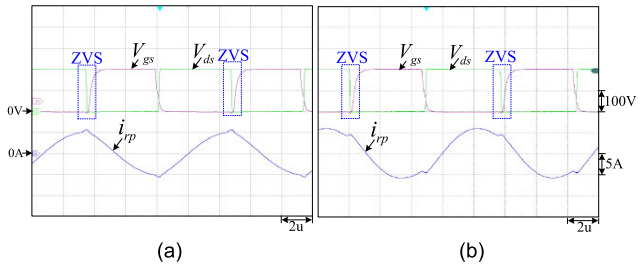

FIGURE 25. Experimental results of ZVS on the high-voltage side under different loaded conditions (V_{dc} = 200 V, V_b = 48 V): (a) 25% rated load; (b) 100% rated load.

2) CHARGING BATTERY

The charging voltage and current command are set at 52 V and 1 C (10.5A), respectively. Turn off the high-voltage electronic load and battery-side DC source. Then, the charging process can be emulated by adjusting the voltage command of the battery-side electronic load from 45 to 53 V. The measured results in Fig. 27 show that CC and CV modes are achieved.

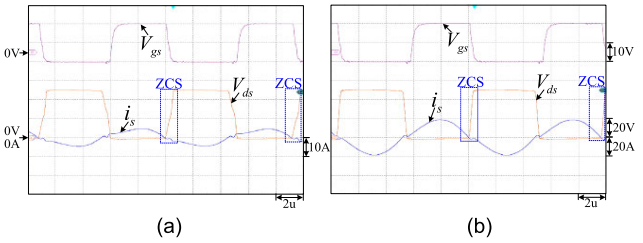

FIGURE 26. Experimental results of ZCS on the low-voltage side under different loaded conditions (V_{dc} = 200 V, V_b = 48 V): (a) 25% rated load; (b) rated load.

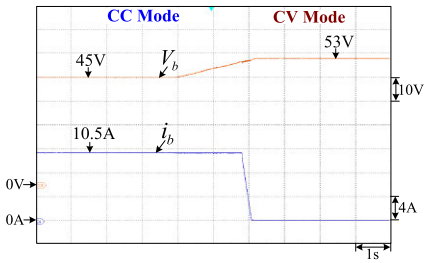

FIGURE 27. Experimental results of charging the battery from the CC to CV mode (V_{dc} = 200 V).

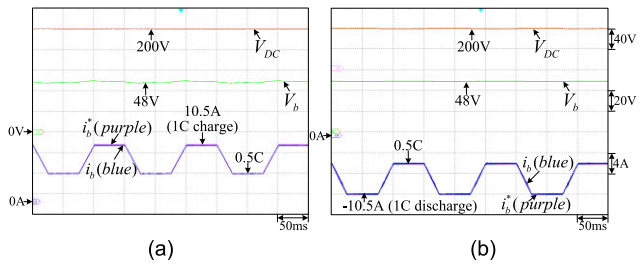

FIGURE 28. Experimental results of current command tracking: (a) charging mode; (b) discharging mode.

3) CURRENT COMMAND TRACKING

Fig. 28 displays the tested results of current command tracking in charging and discharging modes. The results indicate that the proposed current controller could provide a fast current response in the discharging mode for the DC-bus.

4) BIDIRECTIONAL POWER FLOW CONTROL

Let the voltage commands of electronic loads be slightly higher than its DC power, which are set at 200 and 48 V, to emulate the DC-bus and battery to absorb injected power during the bidirectional power flow test. The experimental results in Fig. 29 indicate that currents in both sides could closely track ramp current commands, particularly in the near-zero current command region, and the transient time from charging to discharging mode and vice versa are less than 30 ms.

C. EFFICIENCY

The test conditions are set as 200 V in the high-voltage side, with the low-side voltage being 45, 48, and 52 V to coordinate charging the battery under different state of charge (SOC).

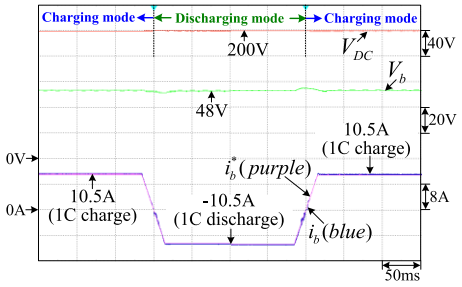

FIGURE 29. Experimental results of the bidirectional power flow test.

1) CHARGING MODE

Fig. 30 presents the experimental results of efficiency with and without the SR, which indicate that the efficiency with SR is higher than 1.5% of the converter without SR. The maximum efficiency is 96% at 52 V and 75% rated load. Moreover, the charging efficiency are more than 92.3% under all tested conditions.

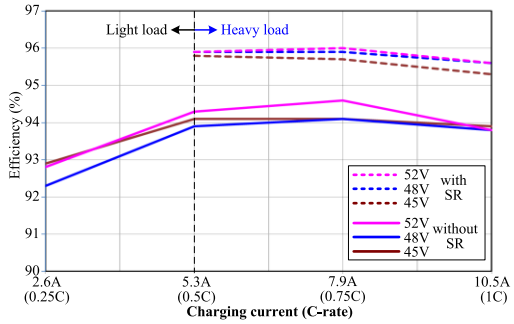

FIGURE 30. Measured efficiency in charging with and without SR.

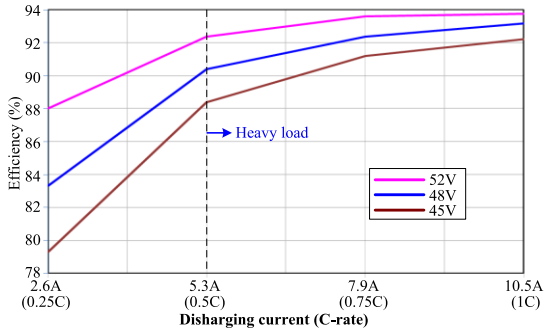

FIGURE 31. Measured efficiency in discharging mode.

2) DISCHARGING MODE

The light load efficiency in Fig. 31 are considerably lower than heavy load conditions because the secondary resonant current with higher secondary magnetizing current is larger in the discharging mode than in the charging mode. The maximum efficiency is 93.8% at 52 V and rated load.

V. CONCLUSION

This paper presents a DSP-based digitally controlled WPT system, including the sandwich structure to match current space and the bidirectional CLLC converter for the e-bike sharing application. The proposed WPT has 500 W of rated power for the bidirectional power flow control to charge and draw electric power from the battery. The efficiency at the rated load is higher than 95.3% in the charging mode and 92% in the discharging mode. The CC/CV charging modes and bidirectional power control are well verified by the proposed experimental platform. Through the simulated results and corresponding analysis, the key contributions of this paper can be summarized as follows:

1) The proposed design process is assisted by simulation tools including Maxwell 3D, MATLAB, and PSIM. Simulated results using Maxwell 3D are verified through experiments, including the effect of the Al outer case and the misalignment of the secondary coil. The maximum errors of coil parameters between the simulation and experiment are less than 6.8%. The simulated results of PSIM and MATLAB to design the CLLC converter match well with experimental results.

2) Because of assistance from Maxwell 3D and the resistance of Litz wires, AWG 44/800 strands that are 2 mm in diameter are used to implement the primary and secondary coils of a circular spiral type under limited space, which could achieve high efficiency and reduce the current rating compared with the other two diameters of Litz wires. Moreover, ferrite pads constructed by eight 53 mm $\times$ 53 mm ferrite pieces with 2.5 mm thickness are adopted to primary coils to achieve high self-inductance and high coupling factor.

3) The maximum error between the simulated and experimental results of charging voltage is less than 6%.

The simulated and experimental results indicate the advantages of the proposed sandwich coil structure as follows:

1) Self-inductance of the primary coil and coupling factor are 116 μH and 0.76, respectively, to provide high mutual inductance. Hence, the magnetizing current is reduced to increase the efficiency of coils.

2) The effect of Z-axis misalignment on the coupling factor and primary self-inductance are nearly zero, and the maximum variation of the coupling factor and self-inductance on the other direction with $\pm$10 mm of misalignment are less than 7%.

REFERENCES

[1] R. B. GmbH, *10 Reasons, for Choosing an eBike*. Baden-Württemberg, Germany: Gerlingen. May 20, 2016. [Online]. Available: https://www.bosch-ebike.com/en/news/10-reasons-for-choosing-an-ebike/

[2] R. B. GmbH. *The Benefits of Commuting With the eBike*. Baden-Württemberg, Germany: Gerlingen. Accessed: Apr. 25, 2017. [Online]. Available: http://www.rutlandcycling.com/content/ebike-commuting.aspx

[3] Statista, Hamburg, Germany. (Mar. 2019). *Number of e-bikes sold in Europe from 2009 to 2018*. [Online]. Available: http://www.eia.gov/Energyexplained/?page=us_energy_transportation

[4] CoMoUK, Leeds, U.K. *Shared Electric Bike Programme Report 2016*. Accessed: 2016. [Online]. Available: https://como.org.uk/wp-content/uploads/2018/05/Shared-Electric-Bike-Programme-Final-Report.pdf

[5] N. McCarthy. (Mar. 2015). *Bike Sharing Schemes: How London Measures Up*. [Online]. Available: https://taipei.youbike.com.tw/use/equipment?5cc296e0083e7b58a8594e02

[6] YouBike Corp., Taipei, Taiwan. *YouBike User Guide*. Accessed: 2020. [Online]. Available: https://taipei.youbike.com.tw/use/equipment?5cc296e0083e7b58a8594e02
[7] Microprogram Information Corp., Taichung, Taiwan. *Bike Sharing System-YouBike*. Accessed: 2018. [Online]. Available: https://www.program.com.tw/en/success/transportation/category/youbike
[8] S. K. J. Chang, H.-Y. Chen, and H.-C. Chen, "Mobility as a service policy planning, deployments and trials in taiwan," *IATSS Res.*, vol. 43, no. 4, pp. 210–218, Dec. 2019.
[9] Citigroup Inc., New York, NY, USA. *Meet the Citi Bike*. Accessed: 2020. [Online]. Available: https://www.citibikenyc.com/how-it-works/electric
[10] P. Rycerski, S. Koutra, K. N. Genikomsakis and Ioakeimidis, "A university survey with a comparative study of an E-bikes sharing system," in *Proc. Symp. Conf.*, Montréal, QC, Canada, Jun. 2016, pp. 1–8.
[11] V. Shevchenko, O. Husev, R. Strzelecki, B. Pakhaliuk, N. Poliakov, and N. Strzelecka, "Compensation topologies in IPT systems: Standards, requirements, classification, analysis, comparison and application," *IEEE Access*, vol. 7, pp. 120559–120580, 2019.
[12] G. R. Mouli, "Solar powered E-bike charging station with AC, DC and contactless charging," in *Proc. Eur. Conf. Power Electron. Appl. (EPE)*, Riga, Latvia, 2018, pp. 1–10.
[13] D. Patil, M. K. McDonough, J. M. Miller, B. Fahimi, and P. T. Balsara, "Wireless power transfer for vehicular applications: Overview and challenges," *IEEE Trans. Transport. Electrific.*, vol. 4, no. 1, pp. 3–37, Mar. 2018.
[14] M. Chinthavali and O. C. Onar, "Tutorial on wireless power transfer systems," in *Proc. IEEE Transp. Electrific. Conf. Expo (ITEC)*, Dearborn, MI, USA, Jun. 2016, pp. 1–142.
[15] *Wireless Power Transfer for Light-Duty Plug-In/Electric Vehicles and Alignment Methodology*, Standard SAEJ2954, May 2016. [Online]. Available: http://standards.sae.org/j2954_201605/
[16] T. M. Fisher, K. B. Farley, Y. Gao, H. Bai, and Z. T. Tse, "Electric vehicle wireless charging technology: A state-of-the-art review of magnetic coupling systems," *Wireless Power Transf.*, vol. 1, no. 2, pp. 87–96, 2014.
[17] D. Maier and N. Parspour, "Wireless Charging—A multi coil system for different ground clearances," *IEEE Access*, vol. 7, pp. 123061–123068, 2019.
[18] S. Li and C. C. Mi, "Wireless power transfer for electric vehicle applications," *IEEE J. Emerg. Sel. Topics Power Electron.*, vol. 3, no. 1, pp. 4–17, Mar. 2015.
[19] Y. Nagatsuka, N. Ehara, Y. Kaneko, S. Abe, and T. Yasuda, "Compact contactless power transfer system for electric vehicles," in *Proc. Int. Power Electron. Conf. (ECCE)*, Sapporo, Japan, Jun. 2010, pp. 807–813.
[20] S. Ahn and J. Kim, "Magnetic field design for high efficient and low EMF wireless power transfer in on-line electric vehicle," in *Proc. 5th Eur. Conf. Antennas Propag. (EUCAP)*, Rome, Italy, 2011, pp. 3979–3982.
[21] R. Severns, E. Yeow, G. Woody, J. Hall, and J. Hayes, "An ultra-compact transformer for a 100 w to 120 kW inductive coupler for electric vehicle battery charging," in *Proc. Appl. Power Electron. Conf. (APEC)*, San Jose, CA, USA, 1996, pp. 32–38.
[22] K. W. Klontz, A. Esser, R. R. Bacon, D. M. Divan, D. W. Novotny, and R. D. Lorenz, "An electric vehicle charging system with 'universal' inductive interface," in *Proc. Conf. Rec. Power Convers. Conf.*, Yokohama, Japan, 1993, pp. 227–232.
[23] C. Song, H. Kim, D. H. Jung, J. J. Kim, S. Kong, J. Kim, S. Ahn, J. Kim, and J. Kim, "Low EMF and EMI design of a tightly coupled handheld resonant magnetic field (HH-RMF) charger for automotive battery charging," *IEEE Trans. Electromagn. Compat.*, vol. 58, no. 4, pp. 1194–1206, Aug. 2016.
[24] C. Liu, C. Jiang, J. Song, and K. T. Chau, "An effective sandwiched wireless power transfer system for charging implantable cardiac pacemaker," *IEEE Trans. Ind. Electron.*, vol. 66, no. 5, pp. 4108–4117, May 2019.
[25] B. Xu, A. Oudalov, A. Ulbig, G. Andersson, and D. Kirschen, "Modeling of lithium-ion battery degradationfor cell life assessment," in *Proc. IEEE Power Energy Soc. Gen. Meeting*, Chicago, IL, USA, Jul. 2017, p. 1.
[26] C. Cai, J. Wang, Z. Fang, P. Zhang, M. Hu, J. Zhang, L. Li, and Z. Lin, "Design and optimization of load-independent magnetic resonant wireless charging system for electric vehicles," *IEEE Access*, vol. 6, pp. 17264–17274, 2018.
[27] M. Budhia, G. A. Covic, and J. T. Boys, "Design and optimization of circular magnetic structures for lumped inductive power transfer systems," *IEEE Trans. Power Electron.*, vol. 26, no. 11, pp. 3096–3108, Nov. 2011.
[28] Y. H. Sohn, B. H. Choi, E. S. Lee, G. C. Lim, G.-H. Cho, and C. T. Rim, "General unified analyses of two-capacitor inductive power transfer systems: Equivalence of current-source SS and SP compensations," *IEEE Trans. Power Electron.*, vol. 30, no. 11, pp. 6030–6045, Nov. 2015.
[29] S. Chatterjee, A. Iyer, C. Bharatiraja, I. Vaghasia, and V. Rajesh, "Design optimisation for an efficient wireless power transfer system for electric vehicles," *Energy Procedia*, vol. 117, pp. 1015–1023, 2017.
[30] R. Bosshard, "Multi-objective optimization of inductive power transfer systems for EV charging," Ph.D. dissertation, Dept. Inf. Technol. Elect. Eng., ETH Zurich, Zürich, Switzerland, 2015.
[31] A. Roßkopf, E. Bär, C. Joffe, and C. Bonse, "Calculation of power losses in litz wire systems by coupling FEM and PEEC method," *IEEE Trans. Power Electron.*, vol. 31, no. 9, pp. 6442–6449, Sep. 2016.
[32] S. Hiruma, Y. Otomo, and H. Igarashi, "Eddy current analysis of litz wire using homogenization-based FEM in conjunction with integral equation," *IEEE Trans. Magn.*, vol. 54, no. 3, pp. 1–4, Mar. 2018. Art no. 7001404
[33] J. M. Miller and A. Daga, "Elements of wireless power transfer essential to high power charging of heavy duty vehicles," *IEEE Trans. Transport. Electrific.*, vol. 1, no. 1, pp. 26–39, Jun. 2015.
[34] Laird Technologies, London, U.K. *Ferrite Plates for Wireless Charging*. Accessed: Jun. 2019. [Online]. Available: https://www.laird.com/wireless-charging/ferrite-plates/mp-33-series-ferrite-plates-wireless-charging
[35] P. He and A. Khaligh, "Comprehensive analyses and comparison of 1 kW isolated DC–DC converters for bidirectional EV charging systems," *IEEE Trans. Transport. Electrific.*, vol. 3, no. 1, pp. 147–156, Mar. 2017.
[36] S. Zou, J. Lu, A. Mallik, and A. Khaligh, "Bi-directional CLLC converter with synchronous rectification for plug-in electric vehicles," *IEEE Trans. Ind. Appl.*, vol. 54, no. 2, pp. 998–1005, Mar. 2018.
[37] S.-Y. Cho, I.-O. Lee, S. Moon, G.-W. Moon, B.-C. Kim, and K. Y. Kim, "Series-series compensated wireless power transfer at two different resonant frequencies," in *Proc. IEEE ECCE Asia Downunder*, Melbourne, VIC, Australia, Jun. 2013, pp. 1052–1058.
[38] G. Liu, Y. Jang, M. M. Jovanovi, and J. Q. Zhang, "Implementation of a 3.3-kW DC–DC converter for EV on-board charger employing the series-resonant converter with Reduced-Frequency-Range control," *IEEE Trans. Power Electron.*, vol. 32, no. 6, pp. 4168–4184, Jun. 2017.
[39] S. Abdel-Rahman. (Sep. 2012). *Resonant LLC Converter: Operation and Design*. [Online]. Available: https://www.infineon.com/dgdl/Application_Note_Resonant+LLC+Converter+Operation+and+Design_Infineon.pdf?fileId=db3a30433a047ba0013a4a60e3be64a1

CHIH-CHIA LIAO (Graduate Student Member, IEEE) received the B.S. degree in electrical engineering from the National Taipei University of Technology, Taipei, Taiwan, in 2014, where he is currently pursuing the Ph.D. degree. His research interests include bidirectional ac-dc/dc-dc converter, wireless power transfer, resonant converter, energy storage systems, power electronics, and digital control.

MING-SHI HUANG (Member, IEEE) received the B.S. degree in electrical engineering from the National Taiwan University of Science and Technology, Taiwan, in 1987, the M.S. degree in electrical engineering from Tatung University, Taiwan, in 1991, and the Ph.D. degree in electrical engineering from National Tsing Hua University, Taiwan, in 2004.

From 1987 to 2004, he was a Researcher with Mechanical Industry Research Laboratories, Industrial Technology Research Institute. He is currently a Professor with the Department of Electrical Engineering, National Taipei University of Technology, Taipei, Taiwan. His areas of research interests include power electronics, variable-speed drives, and electrical power train in vehicle applications.

ZHENG-FENG LI (Graduate Student Member, IEEE) received the B.S. and M.S. degrees in electrical engineering from the National Taipei University of Technology, Taipei, Taiwan, in 2015 and 2017, respectively, where he is currently pursuing the Ph.D. degree. His research interests include resonant converter, wireless power transfer, motor design, and digital control.

FAA-JENG LIN (Fellow, IEEE) received the B.S. and M.S. degrees in electrical engineering from National Cheng Kung University, Taiwan, in 1983 and 1985, respectively, and the Ph.D. degree in electrical engineering from National Tsing Hua University, Taiwan, in 1993. He is currently a Chair Professor with the Department of Electrical Engineering, National Central University, Taiwan. His research interests include ac motor drives, power electronics, renewable energies, smart grids, intelligent, and nonlinear control theories. His work has been widely cited. Several of his articles have helped to establish research areas such as fuzzy neural network control of motor drives and motion control systems, and resonant converters for piezo-ceramic motor drives. He is an IET Fellow. He received the Outstanding Research Awards from the National Science Council, Taiwan, in 2004, 2010, and 2013, and the Outstanding Professor of Engineering Award from the Chinese Institute of Engineers, Taiwan, in 2016. He was an Associate Editor of the IEEE TRANSACTIONS ON FUZZY SYSTEMS. He was the President of the Taiwan Smart Grid Industry Association, from 2012 to 2016, and the Chair and Principle Investigator of Smart Grid Focus Center, National Energy Project Phase I and II in Taiwan, from 2011 to 2019. He is currently an Associate Editor of the IEEE TRANSACTIONS ON POWER ELECTRONICS and the Executive Director of Taiwan Power Company.

WEI-TING WU was born in Taipei, Taiwan, in 1998. He is currently pursuing the B.S. degree with the National Taipei University of Technology, Taipei. His research interests include resonant converter, wireless power transfer, and digital control.